Title

Atomic-scale identification of defects in alite

Authors

Zheng, Qi
Liang, Chengyao
Jiang, Jinyang
et al.

Publication Date

2024-02-01

DOI

10.1016/j.cemconres.2023.107391

Peer reviewed

Atomic-scale Identification of Defects in Alite

Qi Zheng[1,2], Chengyao Liang[1], Jinyang Jiang[3], Haiyan Mao[4], Karen C. Bustillo[5], Chengyu Song[5], Jeffrey A. Reimer[4], Paulo J.M. Monteiro[1], Haimei Zheng[2*], Shaofan Li[1*]

[1]Department of Civil and Environmental Engineering, University of California, Berkeley, California 94720, United States
[2]Materials Science Division, Lawrence Berkeley National Laboratory, Berkeley, CA 94720, United States
[3]School of Materials Science and Engineering, Southeast University, Nanjing 211189, P.R.China
[4]Department of Chemical and Biomolecular Engineering, University of California, Berkeley, Berkeley, CA 94720, United States
[5]National Center for Electron Microscopy, Molecular Foundry, Lawrence Berkeley National Laboratory, Berkeley, CA 94720, United States

ABSTRACT

Crystallographic defects play a crucial role in cement hydration, with initial dissolution being dominated by the formation of etch pits that rely on the intersection of defects on surfaces. However, the defects present in cement particles have remained a mystery due to the lack of direct observation. In this study, we used scanning transmission electron microscopy to unravel the defects in alite particles at the atomic level. Our observations identified different types of defects, including vacancies, doping, dislocations, rough surfaces, and grain boundaries. Atomic ordering in the alite crystal was further examined based on our single-atom recognition method. Our findings indicate that defects in cement particles may serve as reactive sites during early hydration, facilitating the initial dissolution and providing nucleation sites for hydration products. This work provides insights into cement defects at the single-atom level and offers new opportunities in tuning the hydration process through defect engineering of cement particles.

KEYWORDS:

Alite structure, defect, atomic resolution, scanning transmission electron microscopy, hydration mechanisms, sustainable cements

1. Introduction

Since the first Portland cement was patented in 1824 by Joseph Aspdin, there has been a continuous process of evolution in cement process technology and cement itself [1]. At the same time, the cement industry is facing challenges to reduce CO_2 emission and enhance the sustainability of cement production [2]. The use of supplementary cementitious materials (SCMs) to replace part of the clinker in cement is the most successful strategy [3]. However, Portland cement clinker is still, by far, the most important compound of modern cements. Therefore, a comprehensive understanding of clinker chemistry is essential for its further development and will become even more important if, as often desired, the SCMs percentage further increases.

Alite (Ca_3SiO_5) is the dominant phase, constituting around 50% to 70% of Portland cement clinker by mass [4]. It contains minor impurities such as alumina or magnesium oxide [5], being responsible for early-age strength development during hydration of Portland cement. Because of the importance of alite, much research work has been done on the crystal structure of alite in the past century [6–8].

On reaction with water, alite undergoes a dissolution-precipitation process. The initial fast dissolution can be attributed to the solution undersaturation [9], as explained by geochemistry theory [10]. Defects in alite particles serve as the primary sites for dissolution with vacancies and etch pits mainly forming at the intersection of surface defects. However, there have been limited studies on the types of defects in alite and their evolution during hydration. Groves et al. examined the crystalline structure of cement clinkers using transmission electron microscopy [11,12], while Bazzoni et al. further investigated the impact of annealing process on alite structure [13], observing twin bands and planar defects at a moderate resolution. The lack of knowledge regarding these aspects significantly hampers the present perception of clinker chemistry. In the light of the facts, the fundamental understanding of alite structure and its chemistry remains a critical issue. It not only aids in comprehending the hydration mechanisms but also paves the way for developing innovative strategies to produce more sustainable cements.

In this study, we investigate crystallographic defects in alite crystals at the atomic level, using scanning transmission electron microscopy (STEM) and bright-field TEM and selected-area diffraction. Through our analysis, we successfully identified various types of defects, including vacancies, doping, dislocations, and grain boundaries. The presence and characteristics of these defects have implications for the hydration behavior of alite, and our findings offer new prospects for manipulating the hydration process by engineering defects in cement particles.

2. Materials and experiments

Alite synthesis. Tricalcium silicate (C_3S in mineralogical stoichiometric notation, C=CaO, S=SiO_2) was prepared in the following protocol: we used a 3:1 stoichiometric mixture of calcium carbonate ($CaCO_3$) and high-purity quartz powder (SiO_2) purchased from Sigma Aldrich. Some minor impurities (<5% Wt, see **Table 1**) including Al_2O_3, Fe_2O_3, and SO_3 are introduced. Wet milling was processed, then dried at 105 °C for 6 h, before the powders were pressed into pellets, followed by a two-step burning synthesis process [14]. The sample was rapidly cooled down using airflow (pressurized air) and finally ground into grains. Note that in the cement clinker field, C_3S with impurities is commonly referred to as alite.

Powder X-ray diffraction (XRD). The Rigaku Miniflex 6G XRD, a benchtop X-ray diffraction system, was used for mineralogy identification. It used a Cu K alpha radiation (λ = 1.5418 Å) with a 600W X-ray source at 40 kV voltage and 15 mA current. The XRD pattern was collected in 1D mode over the range of 2θ =2-80° (0.02° per step), with a scanning speed of 2°/min.

Transmission electron microscopy (TEM). The Thermo Fisher Scientific ThemIS was used to characterize the morphology at low magnification and to acquire chemical maps. The microscope was operated at 300 keV. A Bruker energy-dispersive X-ray spectroscopy (EDS) detector, with a solid angle of 0.7 steradian, allowed high count rates with minimal dead time for fast EDS mapping. The dwell time was set 20 μs with drift correction enabled. For bright-field imaging, the electron dose rate was ~11 $e \cdot Å^{-2} \cdot s^{-1}$. About EDS analysis, a multi-polynomial model was applied for background correction. Small particles and thin sample edges were used to accurately quantify the elemental ratios. Additionally, we employed an absorption correction by using a sample thickness of 500 nm and a density of ~3.1 $g \cdot cm^{-3}$. Schreiber-Wims function was selected as the ionization cross-section model. All the operations and analysis were done in the Velox software.

High-angle annular dark-field imaging, scanning transmission electron microscopy (HAADF-STEM). Atomic resolution STEM images of alite particles were acquired using a FEI Titan 80-300 (TEAM 0.5) microscope operating at 200 keV. The beam current was set to 70 pA, and the probe semi-angle was set at 25 mrad. The scattered electrons were captured by a Fischione 3000 HAADF detector.

Selected area electron diffraction (SAED). SAED was performed on Tecnai T20 at 200 keV, using Orius SCD200D CCD camera.

Diffraction pattern simulations. CrystalMaker and SingleCrystal software packages were used for visualization of the crystal structures as well as simulating the diffraction patterns at different zone axes with all parameters consistent with the experiment setups. Considering the perfect symmetry in the crystal structure used, some spots in the simulated pattern can be missing due to the extinction effect. These spots can be visible in experiments as natural crystals might display defects to break the symmetries. We indexed the diffraction patterns by comparing the physical distances between spots and the angles between respective spots. The Best-fit pattern with a smallest sum-of-squares error, was considered the optimal indexing.

Table 1. Chemical composition (Wt%) of alite sample from energy-dispersive X-ray spectroscopy. It is noted that Fe, Co, Cu, and Zr likely originate from the pole piece, grid, or detector; Al, S, Cr, and Ni may be present, while Fe and Cu are more likely to be minor constituents based on expected minor constituents.

CaO	SiO_2	CuO	Al_2O_3	NiO	Cr_2O_3	Fe_2O_3	ZrO	CoO	SO_3
73.2	23.4	2.4	0.1	0.3	0.1	0.1	0.2	0.1	0.1

3. Results and discussions

3.1. Identification of M1 alite

Alite exhibits complex polymorphisms that depend on burning temperatures and the type and content of impurities [5]. Previous reports have identified seven polymorphic modifications, including three triclinic (T1, T2, and T3), three monoclinic (M1, M2, and M3) and one rhombohedral (R) structures [15]. Herein, we confirmed the alite sample used corresponds to the monoclinic (M1) crystal form, both from the elemental and structural perspectives. M1 alite is a

typical phase in Portland clinker; we used it as the model system to investigate the defects. **Figure 1A** demonstrates the uniform distribution of calcium (Ca) and silicon (Si) elements in the alite particles analyzed in our work. The Ca/Si ratio, determined from the EDS mapping, is found to be 3.07±0.05, as indicated by the Si-K_{α}, Ca-$K_{\alpha,\beta}$ edges in **Figure 1B**. Additionally, we noticed that some foreign ions are present in alite (**Figure 1C**, also see **Table 1**). Fe, Co, Cu, and Zr are likely from the pole piece, grid, or detector; Al, S, Cr, and Ni are possibly present, while Fe and Cu are more likely to be minor constituents in alite. These minor impurities can have a significant impact on the crystal structure of alite. For instance, S tends to stabilize the M1 alite polymorph, and the presence of Fe^{3+} and Al^{3+} can further facilitate the incorporation of S into the structure [14,16].

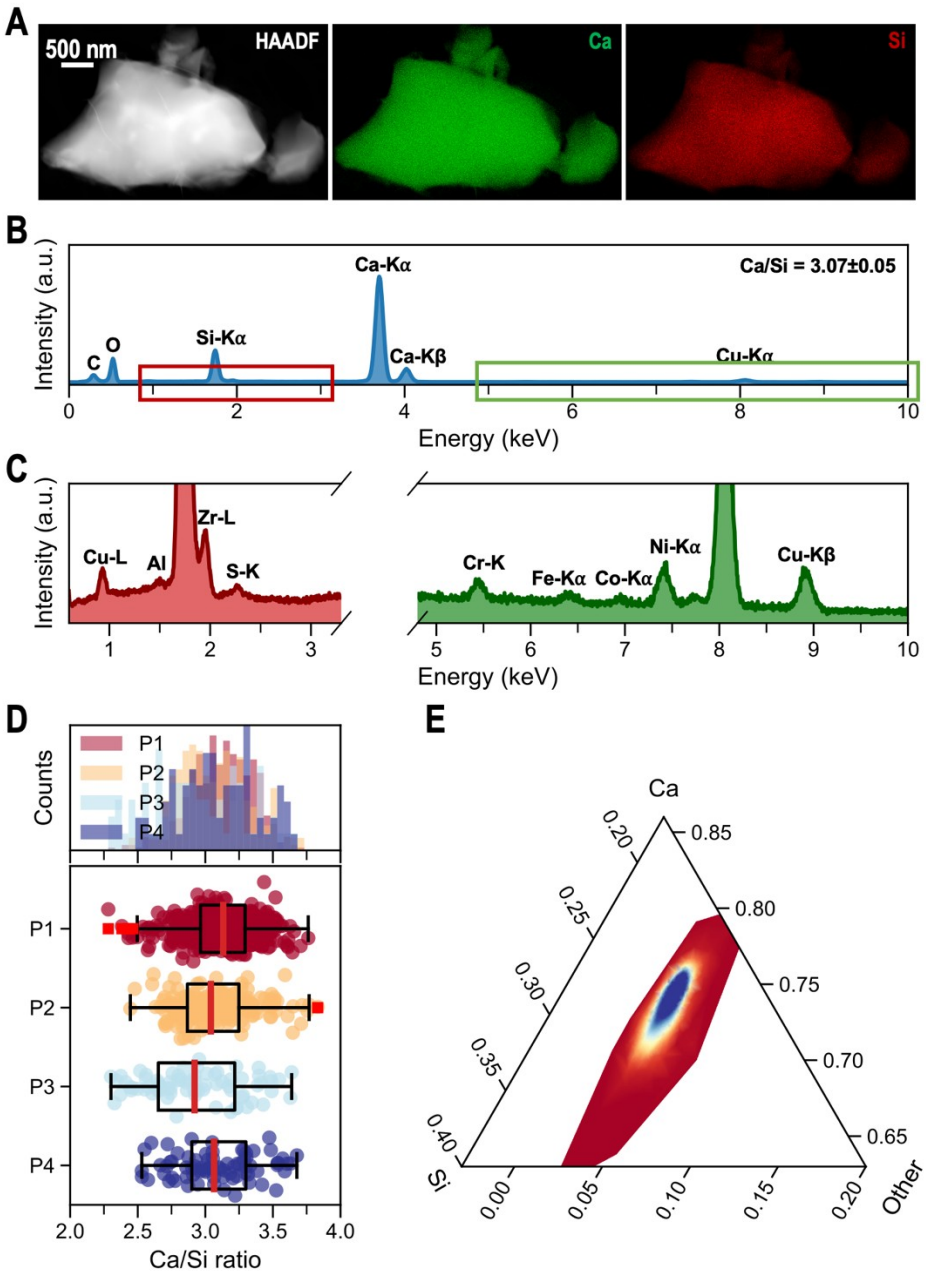

Figure 1. Elemental analysis of alite particles. (**A**) HAADF image and EDS mapping of an alite particle, and (**B**) its corresponding EDS spectrum. (**C**) Magnified EDS spectrum with foreign elements highlighted. (**D**) Ca/Si ratios of four alite batches. (**E**) Ternary plot (At%) of alite particles concerning elements of Ca, Si and other foreign ions (i.e., Al, S, Cr, Ni, etc.).

We conducted detailed elemental analysis on different alite batches (P1-P4). The dots in **Figure 1D** represent the Ca/Si ratios measured from individual alite particles. Here, we focused on particles smaller than 1 μm or thin particle edges to ensure a higher accuracy when measuring the Ca/Si ratios. It was found that alite displays a consistent Ca/Si ratio of approximately 3.1 among different batches (as depicted in Ca/Si distributions in the upper panel). However, it should be noted that certain particles may exhibit higher Ca/Si ratios if surrounded by residual f-CaO [17]. Moreover, the ternary plot analysis in **Figure 1E** provides further support for the reproducibility of current alite synthesis method [14], confirming that the alite sample possesses a similar composition with minor impurities, accounting for approximately 5% atomic percent.
We identified the alite polymorphism as M1-C_3S through Rietveld refinement (**Figure 2A**). The alite crystal used in this work belongs to the monoclinic symmetry. The initial structure was determined from Mumme's diffractometry experiments [18] with consideration of the superstructure modulations with impurities in this work. **Figure 2B** illustrates the ideal unit cell model, where SiO_4 tetrahedra are incorporated within a network of CaO_6 octahedra. Interestingly, realistic M1 alite crystals commonly exhibit orientational disorder of silicate ions in different stacking modes [19], along with superstructure formation induced by substitutions along the *a* axis [20].
The cell dimensions of the revised crystal structure are provided in **Table 2**. We found the fitted cell parameters are in good agreement with the reported values [5,14,15], yielding an acceptable R_{wp} value of < 10%.

Table 2. Unit cell dimensions of M1 alite after Rietveld refinement, in the angular range of 2-80° ($2\theta_{Cu}$).

	a **(Å)**	***b*** **(Å)**	***c*** **(Å)**	**α (°)**	***β*** **(°)**	***γ*** **(°)**	R_{wp}
This work	27.69	7.02	12.21	90	116.03	90	8.15%
Noirfontaine [15]	27.87	7.05	12.26	90	116.03	90	9.25%
Fernandez [5]	27.83	7.06	12.23	90	116.06	90	8.07%
Dvořák [14]	27.89	7.08	12.26	90	116.05	90	6.29%

Selected area electron diffraction (SAED) was carried out on individual alite particles to validate the M1 crystal symmetry of the sample. The SAED patterns of alite collected from various zone axes are shown in **Figure 2C**. These patterns contain spots that can be precisely indexed based on the known crystal structure of M1 alite. Importantly, the experimental diffraction patterns closely match the simulated ones (**Figure 2D**), exhibiting identical *d*-spacing distances and angles between spots. In detail, the (300) facet possesses a *d*-spacing of 2.8 Å, while the spacing of the (020) facet is 3.5 Å [18]. This agreement between the experimental and simulated patterns provides strong evidence supporting the crystal symmetry of M1 alite in the sample.
Meanwhile, the emergence of forbidden reflections (i.e., the (010) spots) in the SAED pattern confirms the monoclinic superstructure of M1 alite. This observation suggests that the crystal

structure of M1 alite might be distorted due to the minor constituents, resulting in the appearance of these forbidden reflections. Additional studies have revealed that trace impurities like ZnO can significantly impact the monoclinic C_3S lattice by influencing the orientational disorder of the SiO_4 tetrahedra [21], which is also a characteristic feature of the alite structure [20,22].

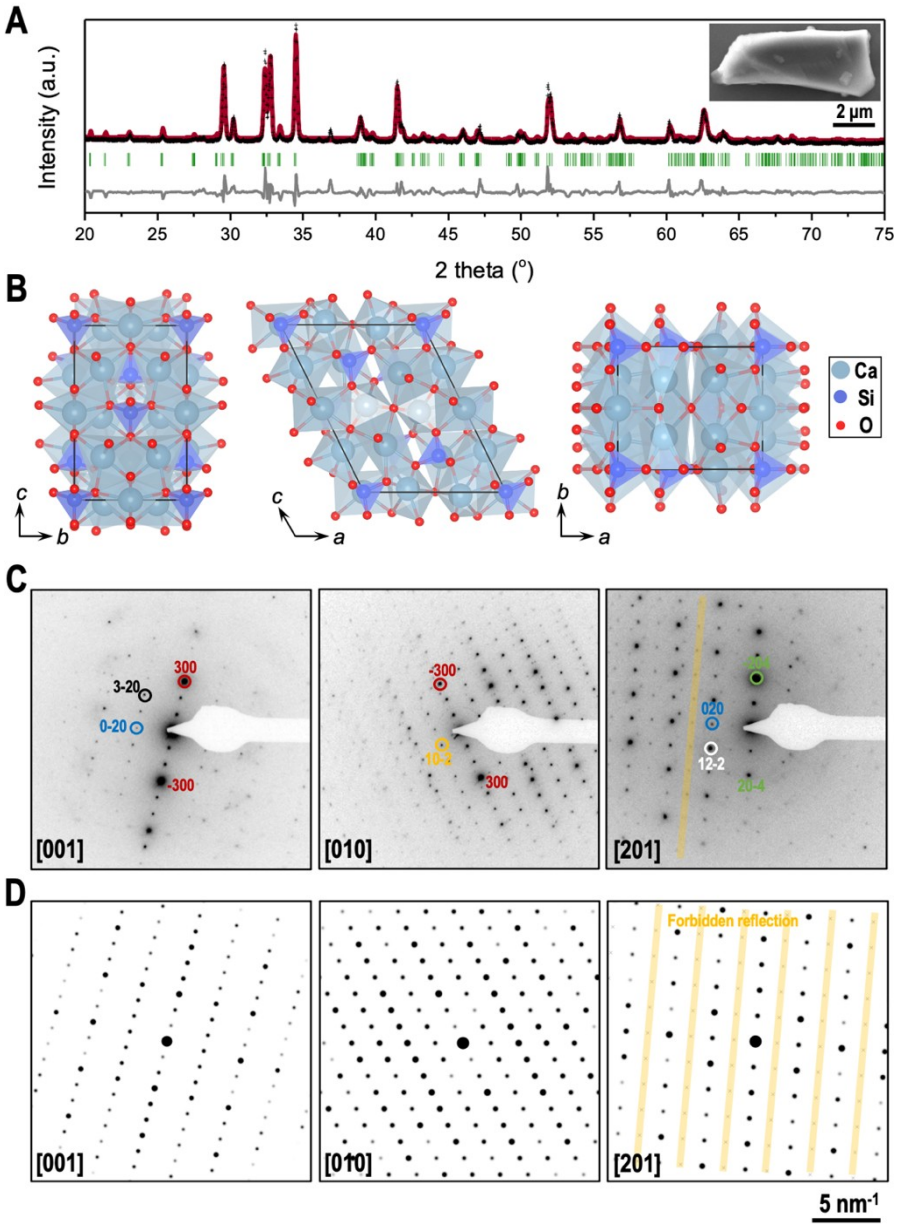

Figure 2. Crystal structure of alite particles. (**A**) XRD and Rietveld analysis results of alite sample. The M1 alite polymorphism was identified (black dots: experimental data; red line: fitted data; green bars: PDF index; grey line: residual error). Inset is a SEM image of an alite particle. (**B**) Refined M1 alite unit structure viewed in different directions. (**C**) Experimental and (**D**) simulated electron diffraction patterns at different view perspectives. Some distinct facets were indexed and highlighted.

3.2. Single-crystalline M1 alite

The alite grains, after the burning and milling processes [23], exhibit irregular shapes with sharp edges (**Figure 3A**). The average size of the alite particles was ~20 μm [24]. For high-resolution STEM characterization, we specifically focused on grains of approximately 1 μm. **Figure 3B** depicts the atomic arrangement of the alite single crystal observed from the [001] direction. It is noted that the Ca atoms can be distinctly identified through some characteristic lattices, including the (040) plane with a spacing of 1.8 Å and the (300) plane with a spacing of 2.8 Å (**Figure 3C**). According to the fast Fourier transform analysis (**Figure 3D** inset) [25], we achieved an unprecedented image resolution of up to 80 pm, a significant achievement in this study. To the best of our knowledge, the image of the alite crystal in this study represents the highest quality attained in the field of cement research. In **Figure 3D**, we captured the rhombic lattice composed of CaO_6 octahedra. The picometer-scale displacements of the CaO_6 octahedra along *x* and *y* directions were further resolved after determining and refining the atom positions (**Figure 3E**) by employing Gonnissen's method [26]. Our findings uncovered atomic heterogeneity in the CaO_6 octahedra, demonstrating their capacity to vibrate and deviate from the equilibrium positions. Consequently, local domains within the crystal may exhibit walls, meanders, and other atomic distortions, which could potentially contribute to the formation of defects in M1 alite.

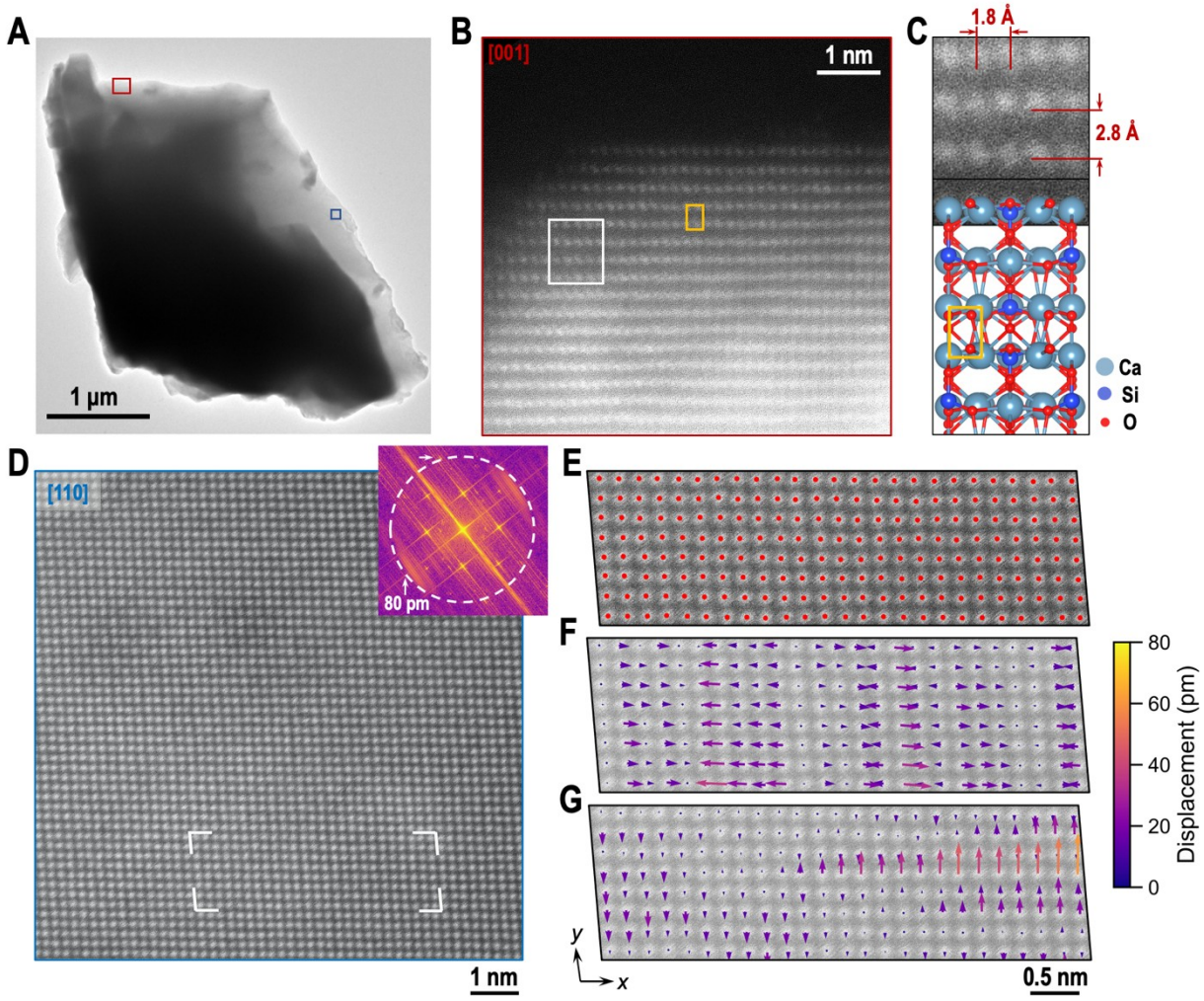

Figure 3. Single-crystalline features of an alite particle. (**A**) An individual alite particle with sharp edges. (**B**) HRSTEM image showing atomic structure of the alite domain observed at [001] zone axis. (**C**) Enlargement of the area in (**B**) overlaid with alite crystal model. (**D**) HRSTEM showing atomic structure of another alite domain observed at [110] zone axis. Inset is its corresponding FFT pattern. (**E**) Enlargement of the area in (**D**) overlaid with recognized atom positions. (**F**) Picometer displacement of atomic positions along *x* and (**G**) *y* directions.

3.3. Defects in M1 alite

In addition to the single-crystalline features in M1 alite, various defects were identified at different scales. Given the uniform thickness of the sample (~50 nm), the contrast of STEM images can be primarily influenced by the atomic number, known as Z-contrast, under the same imaging conditions [27]. Brighter dots in the image indicate atoms with higher atomic mass. **Figures 4A**, **B** illustrate the presence of atomic point defects, specifically vacancies and substitutions, within the M1 alite crystal. To analyze these defects, we calculated intensity profiles of the crystal domain highlighted in **Figures 4A**, **B**. Vacancies were found to manifest as an intensity drop, as shown in **Figure 4C**, while doping with heavy elements such as Cu and Fe substituting the Ca ions, can result in an intensity rise (**Figure 4D**). Interestingly, the atomic vacancies in alite appear characteristics of Schottky defects [28], suggesting that atoms move from the interior to the surface of alite crystal. Furthermore, we observed that both vacancies and substitutions tend to be located on the edges of the crystal. This aligns with the theory that doping occurs dominantly through a diffusion process.

Based on the accumulated evidence, we have developed some alite models with point defects. These models take into consideration both vacancies and substitutions (**Figures 4E**, **F**), providing a more comprehensive description of the alite structure. The substitutions can play different roles: for example, in previous reports, Cu^{2+} ions were found to preferentially substitute Ca sites, while Al^{3+} ions tend to replace Si sites. Fe^{3+} ions, on the other hand, exhibit a preference in occupying the interstitial sites [5]. Moreover, specific description of defects can be valuable for researchers conducting molecular dynamics simulations in silicate systems [30,31], deepening the understanding of alite hydration.

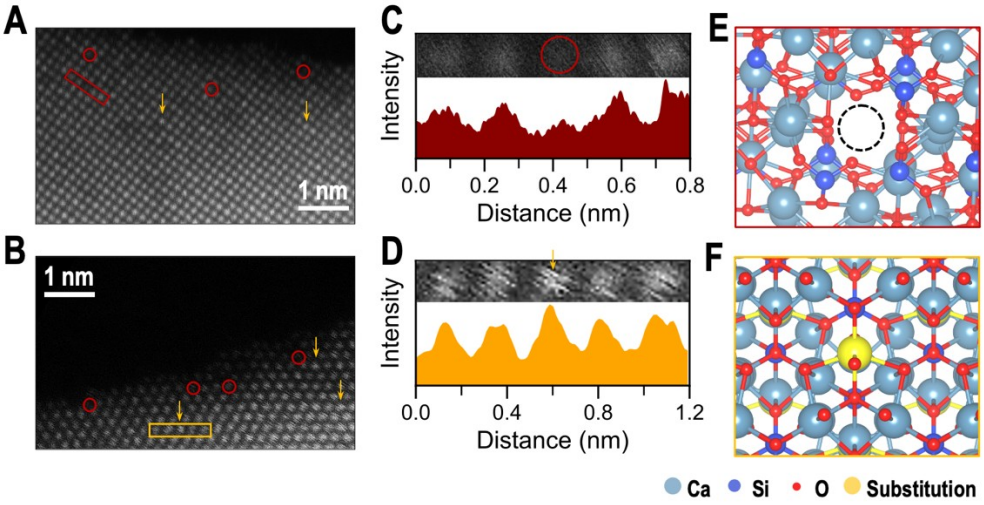

Figure 4. Point defects in alite. (**A**, **B**) Atomic vacancies (circles) and substitutions (arrows). (**C**) Enlargement of the area in (**A**) with its intensity profile. The vacancy can be distinguished by an intensity drop. (**D**) Enlargement of the area in (**B**) with its intensity profile. The substitution can be indicated by an increased intensity. (**E**) An atomistic vacancy model and (**F**) substitution model, observed from [110] and [301] zone axes, respectively.

Figure 5A reveals kink bands in the M1 alite crystal. We mapped the local curvature distribution of the alite layers showing a significant diversity (**Figure 5B**). Additional analysis details can be found in [32]. As alite is produced through a high-temperature process exceeding 1000 °C, the observed structural bending can be attributed to stress-induced phase transformations [33]. External stress can lead to remarkable distortions in the CaO_6 layers, as shown in **Figure 5C**. Other line defects, such as dislocations, were also tracked between the layers (**Figure 5D**). These dislocations can cause rearrangements in the interlayer spacing [34]. Specifically, we found the shrinkage of the spacing from 2.8 to 2.5 Å in the region of dislocation core, while expansion was noticed in the surrounding regions (**Figure 5E**). Given the layered nature of the alite crystal (**Figure 5F**), the presence of dislocations is not surprising. Similar dislocations have been commonly observed in layered oxides [35] and van der Waals crystals [36,37].

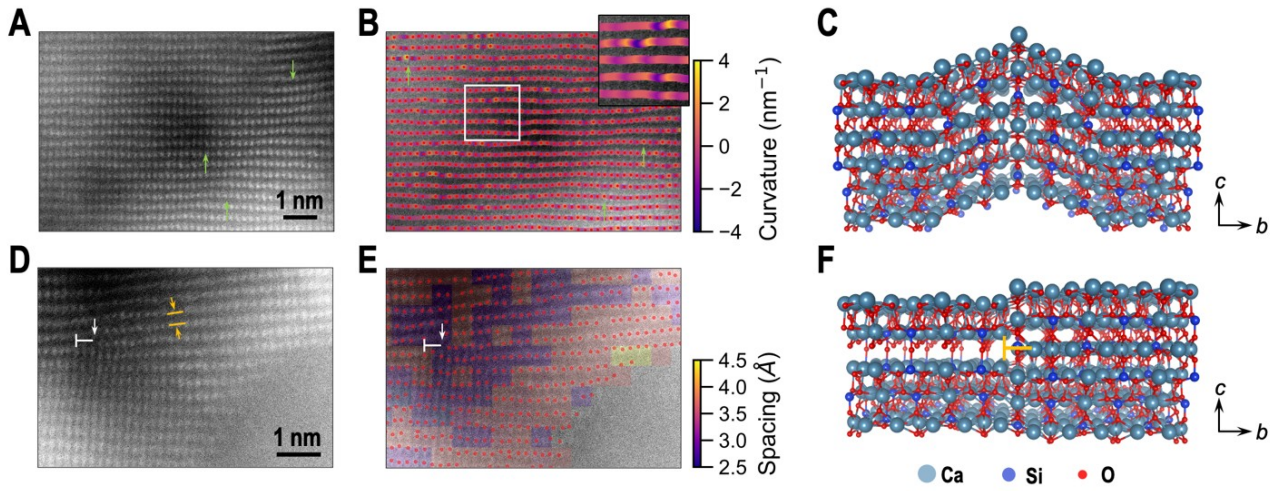

Figure 5. Line defects in alite including kink bands and dislocations. (**A**) Structural bending along the Ca layers, (**B**) calculated local curvature map based on the atom positions, and (**C**) the corresponding atomic model schematic. (**D**) Edge dislocation in alite, (**E**) calculated spacing map, and (**F**) proposed dislocation model.

Furthermore, we observed that the alite particles exhibit rough surfaces at the atomic level, which can be considered as a type of surface defect (**Figure 6A**). The roughness of the surface can be attributed to the grinding and milling processes involved in the synthesis. Typically, zig-zag surface structures are considered unstable [38]. However, we propose that the presence of foreign ions (i.e., Al, S, etc.) may contribute to stabilizing these structures; and they may serve as the initial sites of dissolution, governed by the high surface energy (**Figure 6B**).

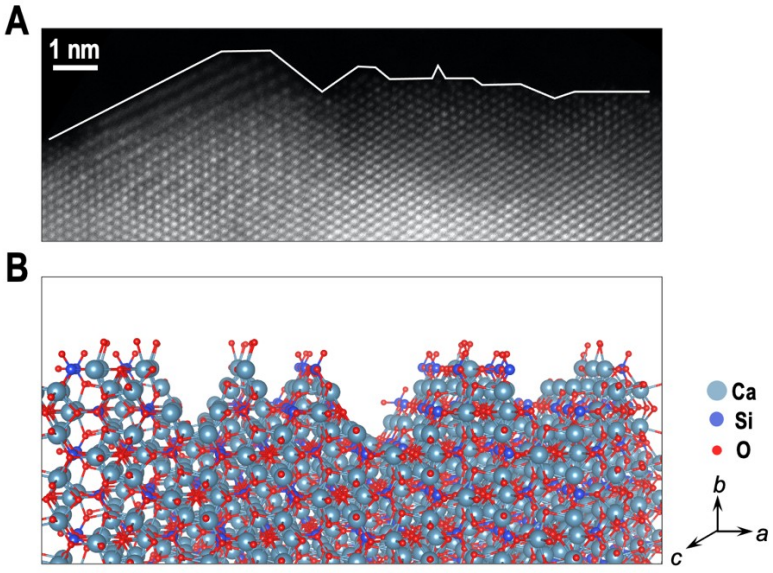

Figure 6. Surface defects in alite, such as rough surfaces with dangling bonds. (**A**) STEM image showing rough surface highlighted in lines. (**B**) A proposed surface model.

Small-scale point, line, and surface defects can potentially evolve into bulk defects. For instance, in **Figure 7A**, single-crystalline alite particles are fused together, forming polycrystals with highlighted grain boundaries. These alite crystals exhibit different orientations and are chemically bonded to adjacent particles. **Figure 7B** illustrates the presence of double helical dislocations possibly facilitated by screw dislocations. It has been reported that a pure screw dislocation can acquire helicity by absorbing point defects during the growth process [39]. Dislocations tend to accumulate near interfaces, impeded by grain boundaries. As they move towards the interface, they encounter resistance and fail to pass through, resulting in a pile-up of dislocations at the grain boundary (**Figure 7C**). High-density dislocations were also observed, forming interconnected networks with localized internal stress (**Figure 7D**). As the density of dislocations increases, these dislocation tangles can transform into dislocation walls at the micrometer scale (**Figure 7E**). Notably, the formation of these dislocation walls gives rise to a long-range dislocation cell structure that spans approximately 2 μm across the entire alite particle. This dramatic dislocation pattern highlights the complex nature of dislocation interactions within the alite crystal lattice.

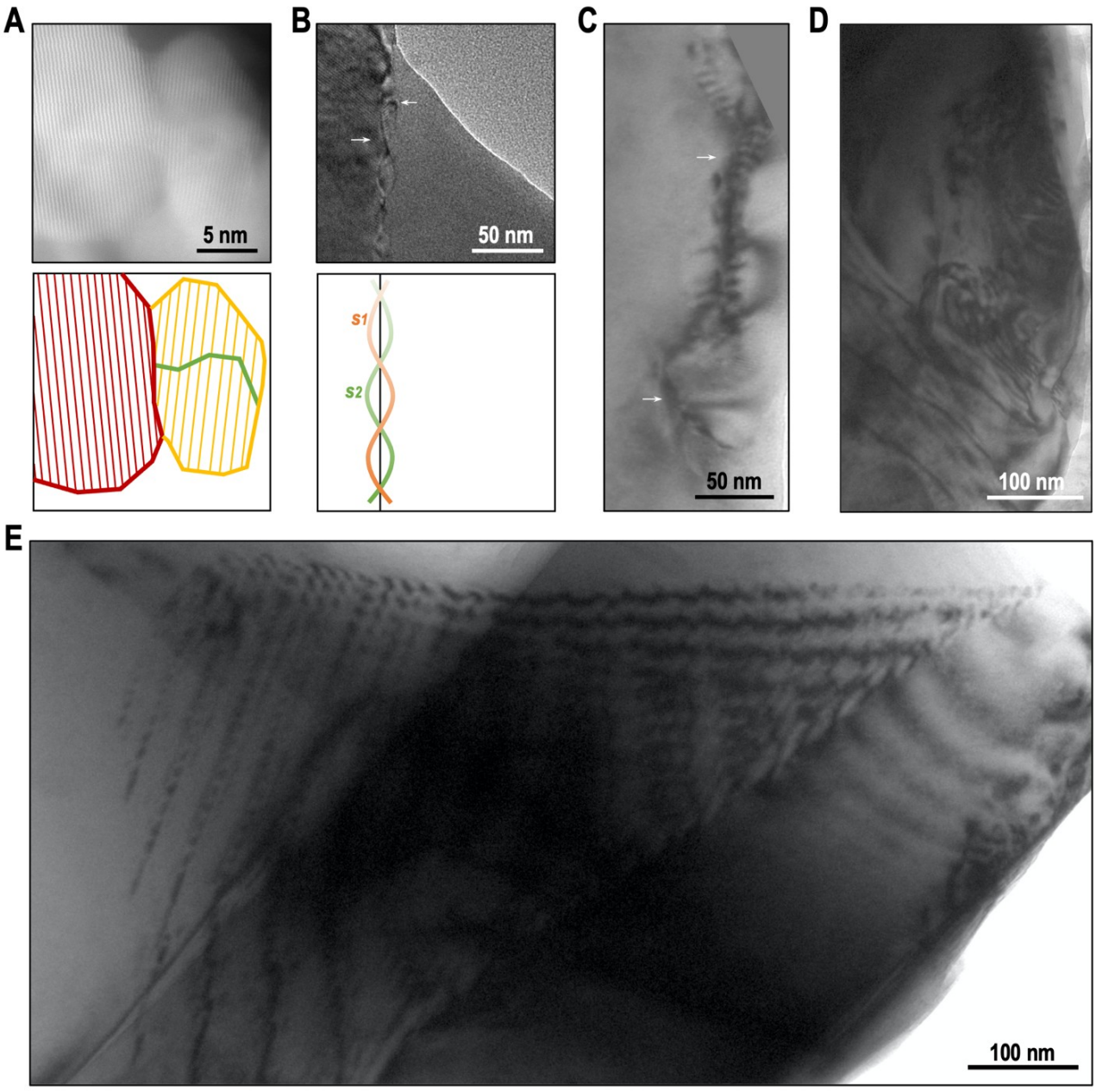

Figure 7. Other defects in alite, such as grain boundaries and dislocation bundles. (**A**) Grain boundaries between alite particles. (**B**) Dislocation network in double helical shape throughout an alite grain. Inset is its corresponding electron diffraction pattern. (**C**, **D**) Dislocation patterns at different densities. (**E**) Long-range dislocation walls.

Crystallographic defects have a significant impact on cement reactions. When cement encounters water, it undergoes rapid dissolution, and the spontaneous formation of hydration products. The defects in cement serve as active sites for the initial dissolution and offer nucleation sites for the subsequent hydration products. The induction period in alite hydration can be explained using the geochemical theory regarding solution undersaturation [9], while the defects in the crystal structure contribute to the rapid dissolution of cement particles within the first few minutes. The

kinetics of dissolution are closely linked to the presence and the density of crystal defects: a higher density of defects can lead to shorter induction periods in cement hydration, as indicated by previous studies [40,41]. Herein, we have identified various defect types in alite crystal at multiple scales, and we have discussed their evolution, which provides new insights into the hydration mechanisms.

4. Conclusions

In this study, we employed transmission electron microscopy to investigate the intrinsic defects present in alite particles.

Based on our findings, the following conclusions can be reached:

(1) At the atomic level, we successfully deciphered point defects such as vacancies and doping within the M1 alite crystal. These defects can arise from the incorporation of substitutional impurities during the calcination process.

(2) Line defects, including edge dislocations and kink bands, were commonly observed in the particles. These defects may have the potential to act as reactive sites for the initial dissolution of alite.

(3) Our analysis revealed that some alite particles exhibit a polycrystalline nature, characterized by distinct grain boundaries. Additionally, we observed a high density of dislocation tangles within the alite particles.

This work provides comprehensive analysis of cement defects at the atomic level, offering insights into their fundamental properties and characteristics. Moreover, it opens up new possibilities for manipulating the hydration process by engineering defects in cement particles.

Acknowledgements

J. Jiang acknowledges the support from the National Natural Science Foundation of China (No. 51925903), the National Key R&D Program of China (2018YFC0705401), State Key Laboratory of High-Performance Civil Engineering Materials Project (2020CEM001), and Science and Technology Research Project of China Railway (2020YY240610, K2020G033). H. Zheng appreciates the support of U.S. Department of Energy (DOE), Office of Science, Office of Basic Energy Sciences (BES), Materials Science and Engineering Division under Contract No. DE-AC02-05-CH11231 within the KC22ZH program. Work at the Molecular Foundry is supported by the Office of Science, Office of Basic Energy Sciences, of the U.S. Department of Energy under Contract No. DE-AC02-05CH11231.

References

[1] H.M. Ludwig, W. Zhang, Research review of cement clinker chemistry, Cem. Concr. Res. 78 (2015) 24–37.

[2] M. Schneider, M. Romer, M. Tschudin, H. Bolio, Sustainable cement production-present and future, Cem. Concr. Res. 41 (2011) 642–650.

[3] K. Scrivener, F. Martirena, S. Bishnoi, S. Maity, Calcined clay limestone cements (LC3), Cem. Concr. Res. 114 (2018) 49–56.

[4] J. Plank, On the correct chemical nomenclature of C_3S, tricalcium oxy silicate, Cem. Concr. Res. 130 (2020) 105957.

[5] W. V Fernandes, S.M. Torres, C.A. Kirk, A.F. Leal, M.R. Lima Filho, D. Diniz,

Incorporation of minor constituents into Portland cement tricalcium silicate: bond valence assessment of the alite M1 polymorph crystal structure using synchrotron XRPD data, Cem. Concr. Res. 136 (2020) 106125.
[6] M. Bigare, A. Guinier, C. Mazieres, M. Regourd, N. Yannaquis, W. Eysbl, T. Hahn, E. Woermann, Polymorphism of tricalcium silicate and its solid solutions, J. Am. Ceram. Soc. 50 (1967) 609–619.
[7] F. Bellmann, J. Leppert, M. Görlach, M. Krbetschek, D. Damidot, H.-M. Ludwig, Analysis of disorder in tricalcium silicate by 29Si NMR spectroscopy and additional methods, Cem. Concr. Res. 57 (2014) 105–116.
[8] Q. Zheng, J. Jiang, X. Li, K.C. Bustillo, H. Zheng, In situ TEM observation of calcium silicate hydrate nanostructure at high temperatures, Cem. Concr. Res. 149 (2021) 106579.
[9] P. Juilland, E. Gallucci, R. Flatt, K. Scrivener, Dissolution theory applied to the induction period in alite hydration, Cem. Concr. Res. 40 (2010) 831–844.
[10] A.C. Lasaga, A. Luttge, Variation of crystal dissolution rate based on a dissolution stepwave model, Science 291 (2001) 2400–2404.
[11] G.W. Groves, Portland cement clinker viewed by transmission electron microscopy, J. Mater. Sci. 16 (1981) 1063–1070.
[12] K.E. Hudson, G.W. Groves, The structure of alite in Portland cement clinker-TEM evidence, Cem. Concr. Res. 12 (1982) 61–68.
[13] A. Bazzoni, M. Cantoni, K.L. Scrivener, Impact of annealing on the early hydration of tricalcium silicate, J. Am. Ceram. Soc. 97 (2014) 584–591.
[14] K. Dvořák, D. Všianský, S. Ravaszová, A. Jančíků, Synthesis of M1 and M3 alite polymorphs and accuracy of their quantification, Cem. Concr. Res. 163 (2023) 107016.
[15] F. Dunstetter, M.-N. De Noirfontaine, M. Courtial, Polymorphism of tricalcium silicate, the major compound of Portland cement clinker: 1. Structural data: review and unified analysis, Cem. Concr. Res. 36 (2006) 39–53.
[16] I. Maki, K. Fukuda, H. Yoshida, J. Kumaki, Effect of MgO and SO3 on the impurity concentration in alite in Portland cement clinker, J. Am. Ceram. Soc. 75 (1992) 3163–3165.
[17] X. Li, A. Ouzia, K. Scrivener, Laboratory synthesis of C3S on the kilogram scale, Cem. Concr. Res. 108 (2018) 201–207.
[18] W.G. Mumme, Crystal structure of tricalcium silicate from a Portland cement clinker and its application to quantitative XRD analysis, (1995).
[19] J.W. Jeffery, The crystal structure of tricalcium silicate, Acta Crystallogr. 5 (1952) 26–35.
[20] F. Nishi, Y. Takeuchi, I. Maki, Tricalcium silicate Ca_3OSiO_4: the monoclinic superstructure, Zeitschrift Für Krist. Mater. 172 (1985) 297–314.
[21] K. Urabe, H. Nakano, H. Morita, Structural modulations in monoclinic tricalcium silicate solid solutions doped with zinc oxide, M (I), M (II), and M (III), J. Am. Ceram. Soc. 85 (2002) 423–429.
[22] M.-N. de Noirfontaine, M. Courtial, F. Dunstetter, G. Gasecki, M. Signes-Frehel, Tricalcium silicate Ca_3SiO_5 superstructure analysis: a route towards the structure of the M 1 polymorph, (2012).
[23] A.K. Chatterjee, Chemistry and engineering of the clinkerization process—Incremental advances and lack of breakthroughs, Cem. Concr. Res. 41 (2011) 624–641.
[24] Q. Zheng, C. Liang, J. Jiang, S. Li, Unveiling the carbonation dynamics of hydrated alite

using electron microscopy, Chem. Eng. J. (2023) 143720.
[25] Z. Chen, Y. Jiang, Y.-T. Shao, M.E. Holtz, M. Odstrčil, M. Guizar-Sicairos, I. Hanke, S. Ganschow, D.G. Schlom, D.A. Muller, Electron ptychography achieves atomic-resolution limits set by lattice vibrations, Science 372 (2021) 826–831.
[26] J. Gonnissen, D. Batuk, G.F. Nataf, L. Jones, A.M. Abakumov, S. Van Aert, D. Schryvers, E.K.H. Salje, Direct observation of ferroelectric domain walls in $LiNbO_3$: wall-meanders, kinks, and local electric charges, Adv. Funct. Mater. 26 (2016) 7599–7604.
[27] S.J. Pennycook, P.D. Nellist, Scanning transmission electron microscopy: imaging and analysis, Springer Science & Business Media, 2011.
[28] S. Mahmoud, P. Carrez, M.L. Dos Reis, N. Mousseau, P. Cordier, Diffusion mechanism of bound Schottky defect in magnesium oxide, Phys. Rev. Mater. 5 (2021) 33609.
[29] R.F. Egerton, Electron energy-loss spectroscopy in the TEM, Reports Prog. Phys. 72 (2008) 16502.
[30] W. Barbosa, T. Honorio, Triclinic tricalcium silicate: Structure and thermoelastic properties from molecular simulations, Cem. Concr. Res. 158 (2022) 106810.
[31] Y. Tao, S. Zare, F. Wang, M.J.A. Qomi, Atomistic thermodynamics and kinetics of dicalcium silicate dissolution, Cem. Concr. Res. 157 (2022) 106833.
[32] Q. Zheng, J. Shangguan, X. Li, Q. Zhang, K.C. Bustillo, L.W. Wang, J. Jiang, H. Zheng, Observation of surface ligands-controlled etching of palladium nanocrystals, Nano Lett. 21 (2021) 6640–6647.
[33] C. Wang, X. Wang, P. Zou, R. Zhang, S. Wang, B. Song, K.-B. Low, H.L. Xin, Direct observation of chemomechanical stress-induced phase transformation in high-Ni layered cathodes for lithium-ion batteries, Matter. 6 (2023) 1265–1277.
[34] Q. Zheng, X. Li, Q. Zhang, D. Lee, H. Mao, C. Yang, K.C. Bustillo, J.A. Reimer, Y. Liu, J. Jiang, A covalent organic framework onion structure, Mater. Today. 60 (2022) 98–105.
[35] A. Singer, M. Zhang, S. Hy, D. Cela, C. Fang, T.A. Wynn, B. Qiu, Y. Xia, Z. Liu, A. Ulvestad, Nucleation of dislocations and their dynamics in layered oxide cathode materials during battery charging, Nat. Energy. 3 (2018) 641–647.
[36] A.P. Rooney, Z. Li, W. Zhao, A. Gholinia, A. Kozikov, G. Auton, F. Ding, R. V Gorbachev, R.J. Young, S.J. Haigh, Anomalous twin boundaries in two dimensional materials, Nat. Commun. 9 (2018) 3597.
[37] D.L. Medlin, N. Yang, C.D. Spataru, L.M. Hale, Y. Mishin, Unraveling the dislocation core structure at a van der Waals gap in bismuth telluride, Nat. Commun. 10 (2019) 1820.
[38] Q. Zheng, X. Shi, J. Jiang, H. Mao, N. Montes, N. Kateris, J.A. Reimer, H. Wang, H. Zheng, Unveiling the complexity of nanodiamond structures, Proc. Natl. Acad. Sci. 120 (2023) e2301981120.
[39] J. Narayan, Discovery of double helix of screw dislocations: a perspective, Mater. Res. Lett. 9 (2021) 453–457.
[40] J.N. Maycock, J. Skalny, R. Kalyoncu, Crystal defects and hydration I. Influence of lattice defects, Cem. Concr. Res. 4 (1974) 835–847.
[41] I. Odler, J. Schüppstuhl, Early hydration of tricalcium silicate III. Control of the induction period, Cem. Concr. Res. 11 (1981) 765–774.